Unconventional Bose-Einstein condensation in a system with two species of bosons in the *p*-orbital bands in an optical lattice

Jhih-Shih You,[1,2] I-Kang Liu,[3] Daw-Wei Wang,[1] Shih-Chuan Gou,[3,*] and Congjun Wu[2,†]

[1]*Physics Department and Physics Division, National Center for Theoretical Sciences, National Tsing-Hua University, Hsinchu 30013, Taiwan*

[2]*Department of Physics, University of California, San Diego, San Diego, California 92093, USA*

[3]*Department of Physics and Graduate Institute of Photonics, National Changhua University of Education, Changhua 50085, Taiwan*

(Received 8 September 2015; published 23 May 2016)

In the context of Gross-Pitaevskii theory, we investigate the unconventional Bose-Einstein condensations in the two-species mixture with p-wave symmetry in the second band of a bipartite optical lattice. An imaginary-time propagation method is developed to numerically determine the p-orbital condensation. Different from the single-species case, the two-species boson mixture exhibits two nonequivalent complex condensates in the intraspecies-interaction-dominating regime, exhibiting the vortex-antivortex lattice configuration in the charge and spin channels, respectively. When the interspecies interaction is tuned across the SU(2) invariant point, the system undergoes a quantum phase transition toward a checkerboardlike spin-density wave state with a real-valued condensate wave function. The influence of lattice asymmetry on the quantum phase transition is addressed. Finally, we present a phase-sensitive measurement scheme for experimentally detecting the unconventional Bose-Einstein condensation in our model.

DOI: 10.1103/PhysRevA.93.053623

I. INTRODUCTION

Unconventional condensate wave functions of paired fermions are identified by nontrivial representations of rotational symmetry, in contrast to the conventional counterpart with vanishing relative orbital angular momentum (OAM). Exploration of unconventional condensates dates back to the investigations of the A and B phases of the superfluid ^{3}He [1–4] and later the spin-triplet pairing in Sr_2RuO_4 [5–8], which are characterized by the formation of Cooper pairs with an OAM of $L = 1$ and a spin triplet of $S = 1$. High-T_c cuprates are another celebrated example whose pairing symmetry is $d_{x^2-y^2}$ [9,10].

Recently, considerable discoveries, both theoretical [11–25] and experimental [26–33], were reported on the single-boson condensation in the metastable high orbital bands of an optical lattice. The wave functions of this archetype of unconventional Bose-Einstein condensation (UBEC) are identified by the nontrivial representations of the lattice symmetry group, which oversteps the physical scenario set by the no-node theorem, an underlying principle of low-temperature physics stating that the many-body ground-state wave functions of Bose systems, including the superfluid, Mott-insulating, and supersolid states, are necessarily positive-definite under general circumstances [18,34]. In consequence, the wave functions of UBECs can be rendered complex valued and thus spontaneously break the time-reversal (TR) symmetry [18], which constitutes a remarkable feature of UBEC. It is anticipated that UBECs can sustain exotic phenomena not seen in conventional BECs, such as the nontrivial ordering of the OAM moment, BECs with nonzero momentum, the half-quantum vortex, and the spin texture of skyrmions [18]. It is also worth mentioning that the OAM moment formation still survives when the system enters the Mott-insulating regime wherein the global U(1) phase coherence of superfluidity is no longer retained [19].

The experimental realization of single-species BECs in the second band, where the condensed atoms survive a long lifetime before tunneling to the nearly empty lowest band [28–32], has marked important progress towards the creation and manipulation of UBECs in ultracold atoms. Depending on the lattice asymmetry, the time-of-flight (TOF) measurement revealed signatures of both real and complex condensates with p-wave symmetry and a large-scale spatial coherence. The complex wave functions exhibit the configuration of a vortex-antivortex lattice with nodal points at vortex cores as theoretically predicted. More recently, a matter-wave interference technique was employed to provide direct observations of the phase information of the condensate and to identify the spatial geometry of certain low-energy excitations [32]. The realization of UBECs in even higher bands was also reported [29,30].

In this work we present a theoretical study of the UBEC in a two-species boson mixture where both species are equally populated in the second band of a bipartite optical lattice [28]. Our study searches for types of UBECs enriched by coupling spin degrees of freedom with U(1) symmetry, TR symmetry, and nontrivial representations of the lattice symmetry groups. To determine the wave function of the UBEC in the context of Gross-Pitaevskii equation (GPE), we develop a numerical scheme that resorts to precluding the s-orbital components from the condensate wave function during the imaginary-time evolution of the full Hamiltonian. This scheme enables us to determine the phase diagram of UBEC in a wide range of parameters corresponding to the interspecies and intraspecies interaction. We find that the emergent phases of UBEC involve the $p_x \pm ip_y$ (complex-valued) and $p_x \pm p_y$ (real-valued) types of orbital order, which appear in different regimes of interaction that can be described as a consequence of the interplay between OAM and interaction energies, as will be discussed later.

This paper is organized as follows. In Sec. II we briefly account for the experimental setup of the bipartite two-

*scgou@cc.ncue.edu.tw

†wucj@physics.ucsd.edu

dimensional lattice potential used in our model, including the symmetry analyses of the lattice configuration. The structure of the single-particle dispersion of the p band is demonstrated. In Sec. III the numerical implementation of the modified imaginary-time propagation method is described, which, together with the Bloch wave approximation, enables us to solve the GPEs in high bands. In Sec. IV we explore the properties of UBECs and phase transitions in the symmetric and asymmetric lattices. A scheme for experimentally exploring the formation of UBECs in our model is addressed in Sec. V. A summary is given in Sec. VI.

II. OPTICAL LATTICE AND BAND SPECTRUM

We consider the two-species BEC in the first excited orbital band of the bipartite optical lattice employed in the experiments [28], where the unit cell consists of two sites with different potential depths. The optical potential $V(x,y)$ is described by

$$V(\mathbf{r}) = -\frac{V_0}{4}|\eta[(\mathbf{e}_z\cos\alpha + \mathbf{e}_z\sin\alpha)e^{ik_l x} + \mathbf{e}_z\epsilon e^{-ik_l x}] + \mathbf{e}_z e^{i\theta}(e^{ik_l y} + \epsilon e^{-ik_l y})|^2, \quad (1)$$

where the unit vectors $\mathbf{e}_z$ and $\mathbf{e}_y$ constitute the basis of the light polarization; V_0 is determined by the laser power; $k_l = 2\pi/a_0$ is the laser wave vector; α is the polarization angle with respect to the z direction; ϵ is the reflection loss, and the intensity and phase differences between laser beams along the x and y directions are described by η and θ, respectively. The symmetry analysis of the lattice configuration and the subsequent band-structure calculations have already been presented in Ref. [19]. Below we recap this analysis in detail to make the paper self-contained.

For the ideal case with $\eta = 1$, $\epsilon = 1$, and $\alpha = 0$, the lattice potential is simplified as

$$V(\mathbf{r}) = -V_0(\cos^2 k_l x + \cos^2 k_l y + 2\cos k_l x \cos k_l y \cos\theta),$$

which possesses the tetragonal symmetry. Since θ controls the relative depth of the double-well inside the unit cell, tuning θ away from 90° results in the bipartite lattice. When $\eta < 1$ and $\epsilon = 1$, the lattice potential becomes

$$V(\mathbf{r}) = -V_0(\eta^2\cos^2 k_l x + \cos^2 k_l y + 2\eta\cos k_l x\cos k_l y\cos\theta),$$

which still possesses the reflection symmetries with respect to both the x and y axes, but the point group symmetry is reduced to the orthorhombic one. For the realistic case with $\eta < 1$ and $\epsilon < 1$, the orthorhombic symmetry is broken such that in general no special point group symmetry survives. Nevertheless, the lattice asymmetry can be partially restored at $\alpha_0 = \cos^{-1}\epsilon$, where the lattice potential becomes

$$V(\mathbf{r}) = -\frac{V_0}{4}\{(1+\eta^2)(1+\epsilon^2) + 2\epsilon^2\eta^2\cos 2k_l x + 2\epsilon^2\eta^2\cos 2k_l y + 4\epsilon\eta\cos 2k_l x[\epsilon\cos(k_l y - \theta) + \cos(k_l y + \theta)]\}$$

and the reflection symmetry with respect to the y axis is retrieved. Therefore, we call the case of α with $\alpha \neq \alpha_0$ asymmetric and that of $\alpha = \alpha_0$ symmetric. The lattice structure

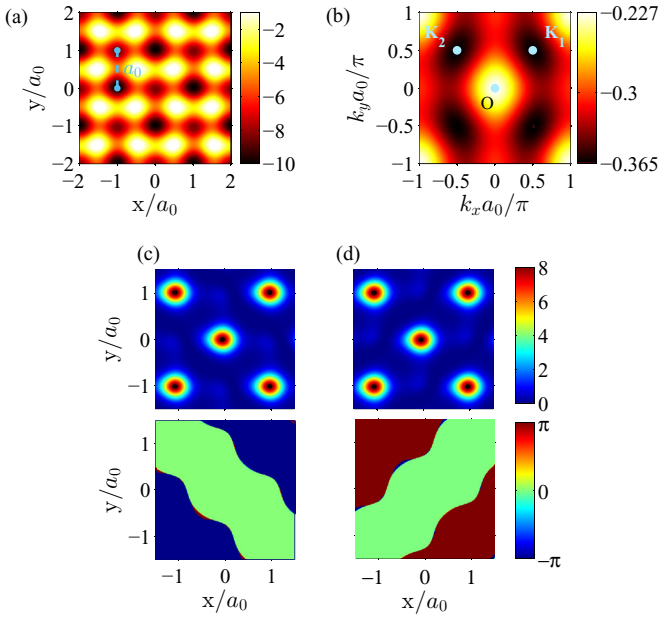

FIG. 1. (a) Double-well optical lattice with the experiment parameters $V_0 = 6.2E_r$, $\eta = 0.95$, $\theta = 95.4^\circ$, $\epsilon = 0.81$, and $\alpha = \pi/5$. The white dashed line illustrates the half wavelength of laser a_0 and $\sqrt{2}a_0$ is the lattice constant. The A and B sublattice sites are shown in (a). (b) Energy spectra of the second band, whose energy minima are located at $\mathbf{K}_1 = (\pi/2a_0, \pi/2a_0)$ and $\mathbf{K}_2 = (-\pi/2a_0, \pi/2a_0)$. (c) and (d) Density profiles (top panels) and phase profiles (bottom panels) for noninteracting gas for (c) $\mathbf{K}_1$ and (d) $\mathbf{K}_2$.

with the experimental parameters $V_0 = 6.2E_r$, $\eta = 0.95$, $\theta = 95.4^\circ$, $\epsilon = 0.81$, and $\alpha = \pi/5$ is shown in Fig. 1(a).

The Bloch wave band structure of the Hamiltonian $H_0 = -\hbar^2\nabla^2/2M + V(\mathbf{r})$ can be calculated based on the plane-waves basis. The reciprocal lattice vectors are defined as $\mathbf{G}_{m,n} = m\mathbf{b}_1 + n\mathbf{b}_2$, with $\mathbf{b}_{1,2} = (\pm\pi/a_0, \pi/a_0)$, where a_0 is the half wavelength of the laser. The diagonal matrix elements are

$$\langle\mathbf{k} + \mathbf{G}_{m,n}|H_0|\mathbf{k} + \mathbf{G}_{m,n}\rangle = E_r\left\{\left[\frac{a_0 k_x}{\pi} + (m-n)\right]^2 + \left[\frac{a_0 k_y}{\pi} + (m+n)\right]^2\right\}, \quad (2)$$

where $\mathbf{k}$ is the quasimomentum in the first Brillouin zone, and the off-diagonal matrix elements are

$$\begin{aligned}
\langle\mathbf{k}|V|\mathbf{k} + \mathbf{G}_{\mp1,0}\rangle &= -\frac{V_0}{4}\epsilon\eta(e^{\pm i\theta} + \cos\alpha e^{\mp i\theta}),\\
\langle\mathbf{k}|V|\mathbf{k} + \mathbf{G}_{0,\pm1}\rangle &= -\frac{V_0}{4}\eta(\epsilon^2 e^{\pm i\theta} + \cos\alpha e^{\mp i\theta}),\\
\langle\mathbf{k}|V|\mathbf{k} + \mathbf{G}_{\mp1,\pm1}\rangle &= -\frac{V_0}{4}\eta^2\epsilon\cos\alpha,\\
\langle\mathbf{k}|V|\mathbf{k} + \mathbf{G}_{\mp1,\mp1}\rangle &= -\frac{V_0}{4}\epsilon.
\end{aligned} \quad (3)$$

The energy spectrum of the second band of the optical lattice [Eq. (1)] is shown in Fig. 1(b). Several observations are in order. First, the energy minima are located at $\mathbf{K}_{1,2} \equiv \mathbf{b}_{1,2}/2$ with the corresponding wave functions $\psi_{\mathbf{K}_1}$ and $\psi_{\mathbf{K}_2}$. For the

symmetric lattice, $\psi_{\mathbf{K}_1}$ and $\psi_{\mathbf{K}_2}$ are degenerate due to reflection symmetry, while for the asymmetric lattice the degeneracy is lifted. Second, there are four points in the Brillouin zone, namely, the zero center O, the high-symmetry point X, $(\pi/a_0,\pi/a_0)$, and $\mathbf{K}_{1,2}$, which are TR invariant because their opposite wave vectors are equivalent to themselves up to reciprocal lattice vectors. As a result, their Bloch wave functions are real; in other words, they are standing waves instead of propagating waves. Third, the hybridized nature of $\psi_{\mathbf{K}_1}$ and $\psi_{\mathbf{K}_2}$ is also manifest in real space: Their wave functions are mostly in the superposition of the local s orbital of the shallow well and the p orbital of the deep well, which possess nodal lines passing through the centers of the deeper wells as shown in Figs. 1(c) and 1(d).

III. MODIFIED IMAGINARY-TIME PROPAGATION METHOD

In current experiments [28], the correlation effects are relatively weak due to the shallow optical potential depth and thus the two-species UBEC can be well described by the coupled GPE as

$$E\Psi_\beta(\mathbf{r}) = \left[H_\beta^0 + \sum_{\alpha=A,B} \tilde{g}_{\beta\alpha}|\Psi_\alpha(\mathbf{r})|^2\right]\Psi_\beta(\mathbf{r}), \tag{4}$$

where $H_\beta^0 = (-\hbar^2\nabla^2)/2M_\beta + V(\mathbf{r})$ is the one-particle Hamiltonian and the wave function Ψ_β is normalized to the area of one unit cell $\int' d^2r|\Psi_\beta(\mathbf{r})|^2 = \Omega = 2a_0^2$; $\tilde{g}_{\alpha\beta} = g_{\alpha\beta}n_\beta$ with n_β the particle number per unit cell and $g_{\alpha\beta}$ the interaction strength between α and β species.

Furthermore, in terms of Ψ_A and Ψ_B, the real-space spin-density distribution is defined as $\mathbf{S}(\mathbf{r}) = (1/2)\Psi^\dagger(\mathbf{r})\hat{\sigma}\Psi(\mathbf{r})$, where $\Psi \equiv (\Psi_A,\Psi_B)^T$ and $\hat{\sigma}$ denotes the Pauli matrices in vector form. Explicitly, the Cartesian components of the spin density are related to Ψ_A and Ψ_B by $S_x + iS_y = \sqrt{2}\hbar\Psi_A^*\Psi_B$ and $S_z = \hbar(|\Psi_A|^2 - |\Psi_B|^2)$. Obviously, the orientation of spin in the xy plane depends only on the global phases of Ψ_A and Ψ_B.

In solving Eq. (4) we assume $\tilde{g}_{AA} = \tilde{g}_{BB}$, $\tilde{g}_{AB} = \tilde{g}_{BA}$, $M_A = M_B = M$ [35,36], and $n_A = n_B$. Since the band minima are located at $\mathbf{K}_{1,2}$, we expand the two-species condensate wave function in terms of $\psi_{\mathbf{K}_1}$ and $\psi_{\mathbf{K}_2}$,

$$\begin{pmatrix}\Psi_A(\mathbf{r})\\ \Psi_B(\mathbf{r})\end{pmatrix} = \begin{pmatrix}\cos\delta_A\psi_{\mathbf{K}_1}(\mathbf{r}) + e^{i\phi_A}\sin\delta_A\psi_{\mathbf{K}_2}(\mathbf{r})\\ \cos\delta_B\psi_{\mathbf{K}_1}(\mathbf{r}) + e^{i\phi_B}\sin\delta_B\psi_{\mathbf{K}_2}(\mathbf{r})\end{pmatrix}. \tag{5}$$

In general, $\psi_{\mathbf{K}_1}(\mathbf{r})$ and $\psi_{\mathbf{K}_2}(\mathbf{r})$ are determined by the renormalized lattice potential and are thus different from those based on the free band Hamiltonian H_0 [37]. Because the particle number of each species is conserved separately, the formation of two-species BEC spontaneously breaks the U(1)×U(1) symmetry, leaving the freedom of choosing the condensate wave function by individually fixing the phase factor of $\psi_{\mathbf{K}_1}(\mathbf{r})$ in each species of Eq. (5).

The theoretical model in the single-species UBEC based on the GP description has been investigated with a self-consistent approach [19,22]. For the two-species case, the structure of competing orders is even richer than that of the single-species case. In the enlarged phase space, the orbital states can entwine with spin degrees of freedom. We introduce a modified imaginary-time propagation method to solve the two-species UBEC, which liberates us from the restriction of certain types of solutions and can be generalized to other higher orbital bands as well. Since the ordinary imaginary-time propagation method only applies to yield the ground-state condensate, in order to reach the UBEC in the second band, the present method is devised to constantly project the lower orbital components out of the evolving (in imaginary time) condensate wave function, forcing the initial wave function evolve to the stationary solution in the target orbital. We have examined this method for one- and two-dimensional harmonic oscillators and the resultant wave functions not only converge to the exact solutions, but also yield the correct degeneracy of high-energy levels.

The implementation of our imaginary-time propagation algorithm is summarized as follows. We start by initializing a trial condensate wave function in the form of Eq. (5) with $\psi_{\mathbf{K}_{1,2}}$ determined by $V(\mathbf{r})$ of the empty lattice. After the propagation of one time step, we arrive at a new set of Ψ_A and Ψ_B, which is then employed to generate the renormalized lattice potential $V_{\mathrm{eff},\alpha}(\mathbf{r}) = V(\mathbf{r}) + \sum_\beta \tilde{g}_{\beta\alpha}|\Psi_\alpha(\mathbf{r})|^2$. Then we solve the s-orbital states $|\varphi_\mathbf{k}\rangle_\alpha$ at $\mathbf{k} = \mathbf{K}_1$ and $\mathbf{K}_2$ based on $V_{\mathrm{eff},\alpha}$ and construct the projection operator

$$\hat{P} = 1 - \sum_{\alpha=A,B}\sum_{\mathbf{k}=\mathbf{K}_1,\mathbf{K}_2} |\varphi_\mathbf{k}\rangle_{\alpha\,\alpha}\langle\varphi_\mathbf{k}|. \tag{6}$$

After projecting out the s-orbital component by applying $\hat{P}$ to $\mathbf{\Psi}$, we proceed to the next step of imaginary-time evolution. The above process is repeated until the convergence is achieved and $\hat{P}$ is updated in each step. To ensure the reliability of this method, we choose several different initial trial wave functions and add small complex random noises to break any specific symmetry that could lock the solution. Every simulation was implemented with a sufficiently long time to ensure that the energy converges. We have successfully reproduced the one-species UBEC solutions in the second band and confirmed the results consistent with the previous works [19,22]. The interaction strengths are much smaller than the energy difference between the s- and p-orbital bands in our simulations and thus the band mixing effect is negligible.

IV. MAIN RESULTS

A. Symmetric lattice

We first consider the symmetric lattice and the competition between intraspecies and interspecies interactions that determines the condensate wave functions. Defining $\gamma = \tilde{g}_{AB}/\tilde{g}_{AA}$, we start with an SU(2) symmetry-breaking case in the regime of $\gamma < 1$. When $\gamma = 0$, the system simply reduces to two decoupled single-species problems and each of them is in the complex condensate exhibiting nodal points rather than nodal lines. Accordingly, there are two p-orbital condensations characterized by substituting the following phase angles into Eq. (5): (I) $\phi_A = \phi_B = \pm\frac{\pi}{2}$ and $\delta_A = \delta_B = \frac{\pi}{4}$,

$$\begin{pmatrix}\Psi_A(\mathbf{r})\\ \Psi_B(\mathbf{r})\end{pmatrix} = \frac{1}{\sqrt{2}}\begin{pmatrix}\psi_{\mathbf{K}_1}(\mathbf{r}) + i\psi_{\mathbf{K}_2}(\mathbf{r})\\ \psi_{\mathbf{K}_1}(\mathbf{r}) + i\psi_{\mathbf{K}_2}(\mathbf{r})\end{pmatrix}, \tag{7}$$

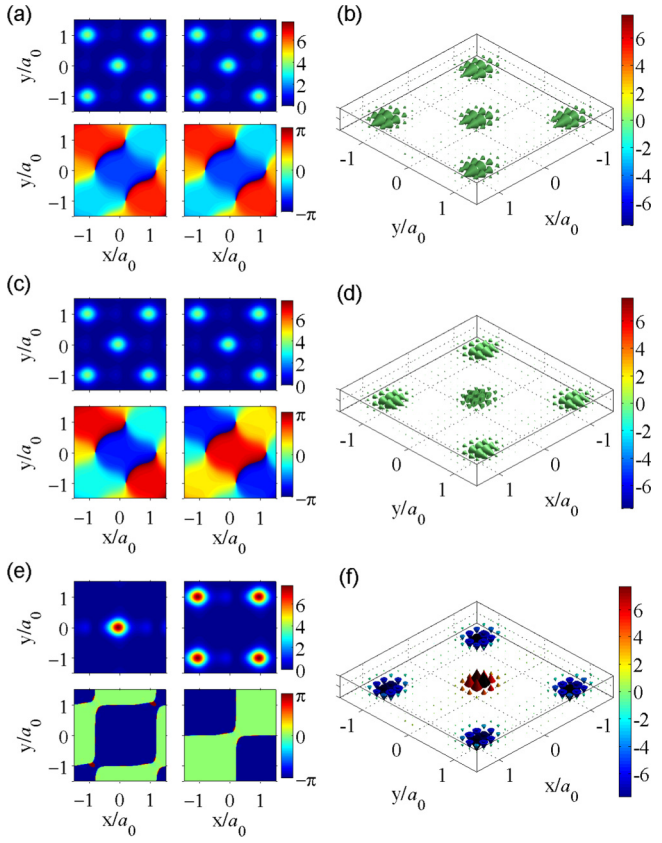

FIG. 2. Spatial distributions of the density, phase, and spin texture of the condensate wave functions corresponding to various states in the symmetric lattice: (a) and (b) state I, (c) and (d) state II, and (e) and (f) the checkerboard state. The intraspecies interactions are $\tilde{g}_{AA} = \tilde{g}_{BB} = 0.025E_r$ with $E_r = \hbar^2 k_l^2/2M$; the interspecies ones are (a) and (b) $\tilde{g}_{AB} = 0.25\tilde{g}_{AA}$ and (c) and (d) $\tilde{g}_{AB} = 1.1\tilde{g}_{AA}$. (a), (c), and (e) Density and phase distributions are shown in the top and bottom panels for each species, respectively. (b), (d) and (f) Spin texture configurations with arrows indicating the orientation of spins and color bars representing the values of S_z. The parameters used are $V_0 = 6.2E_r$, $\eta = 0.95$, $\theta = 95.4^\circ$, $\epsilon = 0.81$, and $\alpha = \alpha_0 = \cos^{-1}\epsilon \approx 35.9^\circ$.

and (II) $\phi_A = -\phi_B = \pm\frac{\pi}{2}$ and $\delta_A = \delta_B = \frac{\pi}{4}$,

$$\begin{pmatrix}\Psi_A(\mathbf{r})\\ \Psi_B(\mathbf{r})\end{pmatrix} = \frac{1}{\sqrt{2}}\begin{pmatrix}\psi_{\mathbf{K}_1}(\mathbf{r}) + i\psi_{\mathbf{K}_2}(\mathbf{r})\\ \psi_{\mathbf{K}_1}(\mathbf{r}) - i\psi_{\mathbf{K}_2}(\mathbf{r})\end{pmatrix}. \tag{8}$$

When $0 < \gamma < 1$, the corresponding p-orbital solutions take the forms of states I and II as well.

States I and II possess different symmetry structures, as illustrated in Figs. 2(a)–2(d). Species A and B can be interpreted as a Kramers doublet and a commonly used Kramers-type TR transformation is defined as $\hat{T} = i\hat{\sigma}_y\hat{C}$, where $\hat{C}$ is the complex conjugation operation and $\hat{\sigma}_y$ is the Pauli matrix. Here $\hat{T}$ keeps the particle number and spin current invariant, but flips the sign of the spin and charge current and satisfies $\hat{T}^2 = -1$. For state I, its axial OAM moments of two species are parallel, exhibiting a vortex-antivortex lattice configuration, and the condensate spin is polarized along the x direction, which obviously breaks the Kramers TR symmetry. As for state II, its axial OAM moments are antiparallel to each other, exhibiting a spin-current vortex-antivortex lattice configuration. Although the spin current is invariant under the Kramers TR transformation, the spin density exhibits the in-plane spin texture with the winding number ± 2 around each vortex core, which also breaks the Kramers TR symmetry. Nevertheless, state II is invariant by the antilinear transformation $\hat{T}' = \hat{\sigma}_x\hat{C}$, which is equivalent to a combination of the TR transformation followed by a rotation around the z axis at π. Since $\hat{T}'^2 = 1$, it is no longer a Kramers transformation, which maintains the xy components of spin invariant but flips the z component of the spin.

States I and II give rise to the same particle density and kinetic energy distributions for both species and thus their energy is degenerate at the mean-field GPE level. Nevertheless, since they are not directly connected by symmetry, this degeneracy is accidental and only valid at the GPE level. The system symmetry allows a current-current interaction between two species, which is absent in the bare Hamiltonian, but could be effectively generated through quantum fluctuations for low-energy physics in the sense of renormalization group. Since the current density distributions of two species are the same in one solution but are opposite in the other, this emergent interaction would lift this accidental degeneracy. However, this is a high-order effect beyond the GPE level, which is certainly an interesting subject for future investigation.

The spatial distributions of the population and phase of both condensate species, together with the corresponding spin texture, are shown in Figs. 2(a) and 2(b), respectively. The particle density is mainly distributed in the shallow sites, which is the nodeless region corresponding to the s orbital, while the density is distributed in the deep sites at which the nodal points are located corresponding to the $p_{x(y)}$ orbitals. Each species exhibits a vortex-antivortex lattice structure: The vortex cores are located at the deep sites and the nodeless region exhibits the quadripartite sublattice structure featuring the cyclic phase factors $\exp(i\pi n/2)$ for $n \in \{1,2,3,4\}$ in the shallow sites. For state I, both species exhibit the same vorticity distribution and thus the spin-density orientation lies along the x direction according to the phase convention of Eq. (5). There is no preferential direction of spin orientation in the xy plane due to U(1) symmetry generated by the total z-component spin. For state II, the two species exhibit opposite vorticities and the configuration is a spin-vortex–antivortex lattice. In both cases, the vorticity or the spin-vorticity patterns exhibit a double period of the lattice potential.

With $\gamma = 1$, the sum of interaction energies is rendered an SU(2)-invariant form such that the wave functions of UBEC become highly degenerate. At this point, states I and II persist as expected. Because of the SU(2) invariance, we can further apply the global SU(2) rotations to states I and II [38]. For state I, the constraint of maintaining $n_A = n_B$ does not allow new states under the form of Eq. (5). For state II, any SU(2) rotation still maintains $n_A = n_B$. For example, after a rotation of $-\pi/2$ around the y axis, we arrive at $(\Psi_A, \Psi_B) = (\psi_{\mathbf{K}_1}, -i\psi_{\mathbf{K}_2})$ and a subsequent $\pi/2$ rotation around the x axis yields

$$\begin{pmatrix}\Psi_A(\mathbf{r})\\ \Psi_B(\mathbf{r})\end{pmatrix} = \frac{1}{\sqrt{2}}\begin{pmatrix}\psi_{\mathbf{K}_1}(\mathbf{r}) + \psi_{\mathbf{K}_2}(\mathbf{r})\\ \psi_{\mathbf{K}_1}(\mathbf{r}) - \psi_{\mathbf{K}_2}(\mathbf{r})\end{pmatrix}. \tag{9}$$

Next we consider the case of $\gamma > 1$, where the degeneracy of the SU(2) invariant condensate wave functions is lifted.

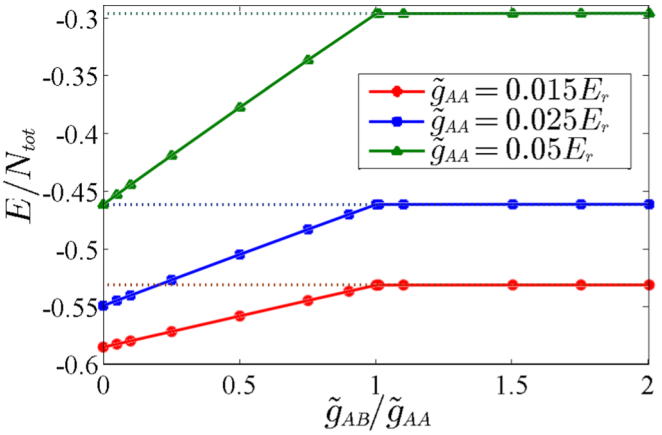

FIG. 3. Plot of $E/N_{\rm tot}$ vs $\tilde{g}_{AB}/\tilde{g}_{AA}$ in the symmetric lattice with $\alpha=\alpha_0$. The red dots, blue triangles, and green squares are for different values of $\tilde{g}_{AA}=0.015E_r$, $0.025E_r$, and $0.05E_r$, respectively. The dashed horizontal line represents the energy for $\gamma>1$ without including domain walls, i.e., solving the GP equation assuming fully polarization. The parameter values are the same as those in Fig. 2.

In this case, within the convention of Eq. (5), the solution of Eq. (9) is selected, whose density, phase, and spin distributions are plotted in Figs. 2(c) and 2(d). We see that bosons of different species occupy mostly the shallow sites in a checkerboard pattern with a staggered spin-density distribution. The condensate wave function in each species becomes real valued with square-shaped nodal lines along with the period-doubled density profile and we call this configuration the checkerboard state. In the single-species case [19,22], the real non-Bloch states $\psi_{\mathbf{K}_1}(\mathbf{r})\pm\psi_{\mathbf{K}_2}(\mathbf{r})$ are always more energetic than the complex non-Bloch states $\psi_{\mathbf{K}_1}(\mathbf{r})\pm i\psi_{\mathbf{K}_2}(\mathbf{r})$ and the real Bloch states $\psi_{\mathbf{K}_1}$ and $\psi_{\mathbf{K}_2}$, because the density distributions of the real non-Bloch states are less uniform than those of the latter. However, the conclusion is opposite in the two-species case: Both species exhibit strong constructive and destructive interferences between $\psi_{\mathbf{K}_1}$ and $\psi_{\mathbf{K}_2}$ alternatively in adjacent shallow sites and their real-space density distributions avoid each other and exhibit the checkerboard pattern. Consequently, the dominant interspecies interaction is greatly suppressed and the checkerboard state turns out to be the least energetic.

In the strongly repulsive regime ($\gamma>1$), however, it is possible that the system develops isolated ferromagnetic single-species domains. The case of spatial separation has been discussed for the bosonic mixture in the s-orbital bands of optical lattices in the same interaction regime [39–42]. When this scenario occurs in p-orbital bands, isolated domains of either species can choose themselves in whichever of the complex states $\psi_{\mathbf{K}_1}(\mathbf{r})\pm i\psi_{\mathbf{K}_2}(\mathbf{r})$. We call such a configuration the spatially phase-separated spin-polarized state. Seemingly, this state could have an energy lower than that of the checkerboard state because of the vanishing interspecies interaction. In Fig. 3 we plot $E/N_{\rm tol}$ of full spin-polarized state with the complex condensate $\psi_{\mathbf{K}_1}(\mathbf{r})+i\psi_{\mathbf{K}_2}(\mathbf{r})$ or its TR breaking counterpart. A simple numerical test shows that the energy per particle of the checkerboard state is very close to that of the fully spin-polarized state. When the initial state is prepared with $n_A=n_B$, the fully spin-polarized state becomes phase-separated spin polarization accompanied by the formation of inhomogeneous ferromagnetic domains, which cost the domain energy. In spite of that, the checkerboard state of Eq. (9) is still the prevailing UBEC state in this regime. Another issue is the time scale: Starting from the unpolarized initial state, forming ferromagnetic domains is a process of phase separation with a large-scale arrangement of real-space boson configurations. It is much longer than the time scale of the formation of the checkerboard state, which only needs local phase adjustment of boson configurations.

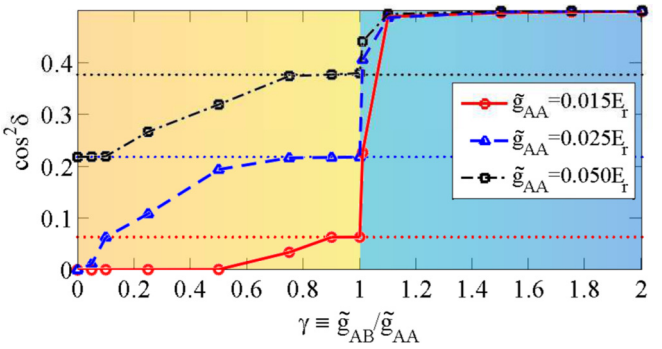

FIG. 4. Condensate fraction of $\psi_{\mathbf{K}_1}$, $\cos^2\delta$, as a function of $\gamma=\tilde{g}_{AB}/\tilde{g}_{AA}$. The red dots, blue triangles, and green squares indicate $\tilde{g}_{AA}/E_r=0.015$, 0.025, and 0.05, respectively, and the dotted lines depict the fraction of spin-polarized state with the same total particle numbers for each interaction strength. The parameter values of the optical lattice here are the same as for Fig. 2 except for $\alpha=\pi/5>\alpha_0$.

B. Asymmetric lattice

Next we consider the interplay between lattice asymmetry and interactions. The lattice asymmetry breaks the degeneracy between the single-particle states $\psi_{\mathbf{K}_1}$ and $\psi_{\mathbf{K}_2}$. Without loss of generality, we choose $\alpha>\alpha_0$, which sets the energy of $\psi_{\mathbf{K}_2}$ slightly lower than that of $\psi_{\mathbf{K}_1}$ such that the calculated condensate wave functions satisfy $\delta_A=\delta_B=\delta\neq\pi/4$. In Fig. 4, the condensate fraction of $\psi_{\mathbf{K}_1}$, $\cos^2\delta$, is plotted as a function of γ at various values of $\tilde{g}_{AA}$. We find that the lattice asymmetry effect is more prominent for weak interactions. At $\tilde{g}_{AA}=0.015E_r$, the condensate fraction of $\psi_{\mathbf{K}_1}(\mathbf{r})$ vanishes when $\gamma<0.5$. The corresponding density, phase, and spin-density distributions are depicted in Figs. 5(a) and 5(b). This is a real Bloch-type UBEC with a stripelike

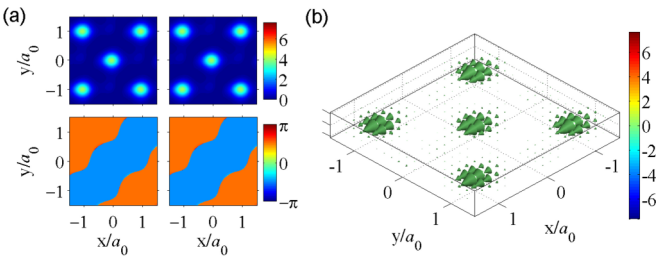

FIG. 5. (a) Density and phase and (b) spin texture of $\tilde{g}_{AA}=\tilde{g}_{BB}=0.015E_r$, and $\gamma=0.1$. The parameter values of the optical lattice here are the same as for Fig. 1 except for $\alpha=\pi/5$.

configuration and an in-plane spin orientation. With increasing γ, $\psi_{\mathbf{K}_1}$ and $\psi_{\mathbf{K}_2}$ superpose in a complex way with $\phi_A = \phi_B = \pm\pi/2$ or $\phi_A = -\phi_B = \pm\pi/2$, but $\cos^2\delta$ remains small even at $\gamma = 1$. We note that only when $\gamma > 1$ does the condensate quickly evolve to the checkerboard state. As $\tilde{g}_{AA}$ increases, the complex non-Bloch condensates become more and more prominent, as shown in Fig. 4.

Hitherto, we have concluded that the two-species p-orbital condensation can manifest itself in different forms of non-Bloch condensation: the complex states I and II, the real checkerboard state in Eq. (9), and the spatially phase-separated spin-polarized state. Since all these states are linear combination of $\psi_{\mathbf{K}_1}(\mathbf{r})$ and $\psi_{\mathbf{K}_2}(\mathbf{r})$, it is expected that four Bragg maxima would develop around the quasimomenta, $\pm\mathbf{K}_{1,2}$ in the TOF spectra [12,19,28]. Given the condensate fractions $\psi_{\mathbf{K}_1}$ of Fig. 4, states I and II as well as the spatially phase-separated complex spin-polarized state show that the relative intensities of these two pairs of peaks are dependent on the lattice asymmetry. However, when $\gamma > 1$, the condensate fractions of $\psi_{\mathbf{K}_1}$ and $\psi_{\mathbf{K}_2}$ for the real checkerboard state quickly become nearly equally populated and thus the Bragg peaks of the TOF spectra have almost equal intensities, irrespective of the lattice asymmetry. This experimental observation could directly exclude the phase-separated spin-polarized state and provide supporting evidence for the phase transition from the complex UBECs towards the real-valued UBEC driven by the interspecies interaction.

V. EXPERIMENTAL SCHEME FOR PHASE MEASUREMENT

The two-species UBEC can be realized and observed by state-of-the-art experimental techniques [28–32]. Utilizing two different hyperfine spin states of an atom (labeled as the A and B species) [35,36], one first creates a condensate of sole species in the superposition of $\psi_{\mathbf{K}_1}(\mathbf{r})$ and $\psi_{\mathbf{K}_2}(\mathbf{r})$, which are the degenerate lowest-energy states in the p-orbital band. A $\pi/2$ Raman pulse is applied to convert half of the already condensed atoms into the other species. After tuning the interspecies atomic interaction with Feshbach resonance, the system is held for some time to let it relax to the intended non-Bloch p-orbital states $\Psi_{A,B} = \psi_{\mathbf{K}_1} + e^{i\phi_{A,B}}\psi_{\mathbf{K}_2}$, whose phase information can be inferred by matter-wave interferometry as explained below.

After the preparation of the two-species condensate, the atoms are then released from optical lattices and subsequently experience a Stern-Gerlach splitting during the ballistic expansion. Precisely, by applying a pulsed magnetic field gradient, the atoms are accelerated by a spin-dependent force [43] $\mathbf{F}_\beta \propto m_\beta |B|\hat{z}$ (m_β is the projection of spin) and thus the two-species UBEC breaks into spatially separated parts along the z direction. A second $\pi/2$ Raman pulse is then applied to mix states of different momenta, leading to

$$\begin{pmatrix}\tilde{\Psi}_A\\ \tilde{\Psi}_B\end{pmatrix} \propto (\psi_{\mathbf{K}_1} + e^{i\phi_A}\psi_{\mathbf{K}_2})\begin{pmatrix}1\\ ie^{i\Phi}\end{pmatrix}\otimes|\mathbf{p}_A\rangle + (\psi_{\mathbf{K}_1} + e^{i\phi_B}\psi_{\mathbf{K}_2})\begin{pmatrix}ie^{-i\Phi}\\ 1\end{pmatrix}\otimes|\mathbf{p}_B\rangle, \quad (10)$$

where Φ accounts for the accumulated phases for the dynamical effects involved and $\mathbf{p}_{A,B}$ denote the momenta acquired by atoms after the Stern-Gerlach splitting. At this stage, the motion of each species is described by a wave packet consisting of a superposition of two non-Bloch states with different quasimomenta that interfere with each other along the z direction during the TOF [32,43]. The phase difference $\Delta\phi_{AB} = \phi_A - \phi_B$ can be inferred from the interference patterns imaged along vertical and horizontal directions for each species, as demonstrated in [32]. It can be shown from Eq. (10) that among the Bragg maxima, the $\mathbf{K}_1$ and $\mathbf{K}_2$ columns possess the same interference pattern, except the positions of fringes in the two columns are shifted by a phase angle $|\Delta\phi_{AB}|$. By comparing the positions of fringes in the Bragg peaks, one can expect, when $\gamma < 1$, $|\Delta\phi_{AB}| = 0$ for state I and $|\Delta\phi_{AB}| = \pi$ for state II. Our scheme provides a feasible way for phase measurement in the current system.

VI. CONCLUSION

In summary, we have studied the two-species p-orbital BECs in the experimentally accessible regime using an imaginary-time propagation method for coupled GPEs, which can be applied to solve UBECs in higher bands. The competition between interspecies and intraspecies interactions drives the transition from two nonequivalent complex-valued states, possessing, respectively, broken and unbroken TR symmetry, to a real-valued checkerboard state with a staggered spin-density structure. We have also proposed experimental schemes to study the UBECs of the mixture. The current study paves the way for approaching the least explored p-orbital physics of multispecies bosonic systems. Our theory can be generalized to study also the superfluity and magnetism of spinful p-orbital condensation in the presence of spin-dependent optical lattices or exotic spin-exchange interactions.

We have used the GPE method throughout this article, whose applicability is justified in the limit of the weak interspecies interaction. In this case, the two-species problem studied here is reduced to two weakly coupled single-species problems, for which previous works show that the GPE has captured the essential physics of the complex p-orbital condensates being the energy minima. When the interspecies interaction becomes stronger, however, the entanglement between two species would become important. In this case, indeed, more exotic states beyond the GPE level are also possible. For example, the singlet paired boson condensation, whose spatial pair wave functions are antisymmetrized, thus reduces the interspecies repulsion. This state is highly entangled and beyond the GPE level. Nevertheless, the mean-field GPE is still a natural beginning point of this challenging problem. The checkerboard state investigated in this article remains a potential competing state; both species avoid each other in their real-space density distributions characterized by a staggered spin-density structure, which also greatly reduces the interspecies repulsion. We leave a detailed study of novel states beyond the mean-field GPE level and their competitions with the single-boson condensate for a future investigation.

ACKNOWLEDGMENTS

J.-S.Y. was supported by the Ministry of Science and Technology, Taiwan (Grant No. MOST 102-2917-I-007-032). I.-K.L. and S.-C.G. were supported by the Ministry of Science and Technology, Taiwan (Grant No. MOST 103-2112-M-018- 002-MY3). S.-C.G. was also supported by the National Center for Theoretical Sciences, Taiwan. C.W. was supported by NSF Grant No. DMR-1410375 and AFOSR Grant No. FA9550-14-1-0168. C.W. acknowledges support from President's Research Catalyst Award No. CA-15-327861 from the University of California Office of the President. We also acknowledge M.-S. Chang for his comments on the proposed experimental scheme.

[1] P. W. Anderson and P. Morel, Phys. Rev. **123**, 1911 (1961).
[2] W. F. Brinkman, J. W. Serene, and P. W. Anderson, Phys. Rev. A **10**, 2386 (1974).
[3] R. Balian and N. R. Werthamer, Phys. Rev. **131**, 1553 (1963).
[4] A. J. Leggett, Rev. Mod. Phys. **47**, 331 (1975).
[5] Y. Maeno *et al.*, Nature (London) **372**, 532 (1994).
[6] A. P. Mackenzie and Y. Maeno, Rev. Mod. Phys. **75**, 657 (2003).
[7] K. D. Nelson, Science **306**, 1151 (2004).
[8] F. Kidwingira, J. D. Strand, D. J. V. Harlingen, and Y. Maeno, Science **314**, 1267 (2006).
[9] D. A. Wollman *et al.*, Phys. Rev. Lett. **71**, 2134 (1993).
[10] C. C. Tsuei *et al.*, Phys. Rev. Lett. **73**, 593 (1994).
[11] A. Isacsson and S. M. Girvin, Phys. Rev. A **72**, 053604 (2005).
[12] W. V. Liu and C. Wu, Phys. Rev. A **74**, 013607 (2006).
[13] C. Wu, W. V. Liu, J. E. Moore, and S. Das Sarma, Phys. Rev. Lett. **97**, 190406 (2006).
[14] A. B. Kuklov, Phys. Rev. Lett. **97**, 110405 (2006).
[15] V. M. Stojanović, C. Wu, W. V. Liu, and S. Das Sarma, Phys. Rev. Lett. **101**, 125301 (2008).
[16] A. Collin, J. Larson, and J. P. Martikainen, Phys. Rev. A **81**, 023605 (2010).
[17] X. Li, E. Zhao, and W. V. Liu, Phys. Rev. A **83**, 063626 (2011).
[18] C. Wu, Mod. Phys. Lett. B **23**, 1 (2009).
[19] Z. Cai and C. Wu, Phys. Rev. A **84**, 033635 (2011).
[20] J.-P. Martikainen, Phys. Rev. A **83**, 013610 (2011).
[21] Z. Cai, L.-M. Duan, and C. Wu, Phys. Rev. A **86**, 051601 (2012).
[22] Y. Xu *et al.*, Phys. Rev. A **87**, 013635 (2013).
[23] B. Liu, X.-L. Yu, and W.-M. Liu, Phys. Rev. A **88**, 063605 (2013).
[24] F. Hébert *et al.*, Phys. Rev. B **87**, 224505 (2013).
[25] X. Li, A. Paramekanti, A. Hemmerich, and W. V. Liu, Nat. Commun. **5**, 3205 (2014).
[26] J. Sebby-Strabley, M. Anderlini, P. S. Jessen, and J. V. Porto, Phys. Rev. A **73**, 033605 (2006).
[27] T. Müller, S. Fölling, A. Widera, and I. Bloch, Phys. Rev. Lett. **99**, 200405 (2007).
[28] G. Wirth, M. Ölschläger, and A. Hemmerich, Nat. Phys. **7**, 147 (2011).
[29] M. Ölschläger, G. Wirth, and A. Hemmerich, Phys. Rev. Lett. **106**, 015302 (2011).
[30] M. Ölschläger, G. Wirth, T. Kock, and A. Hemmerich, Phys. Rev. Lett. **108**, 075302 (2012).
[31] M. Ölschläger *et al.*, New J. Phys. **15**, 083041 (2013).
[32] T. Kock *et al.*, Phys. Rev. Lett. **114**, 115301 (2015).
[33] D. Hu, L. Niu, B. Yang, X. Chen, B. Wu, H. Xiong, and X. Zhou, Phys. Rev. A **92**, 043614 (2015).
[34] R. P. Feynman, *Statistical Mechanics, A Set of Lectures* (Addison-Wesley, Reading, 1972).
[35] C. J. Myatt *et al.*, Phys. Rev. Lett. **78**, 586 (1997).
[36] D. S. Hall *et al.*, Phys. Rev. Lett. **81**, 1539 (1998).
[37] Here we have assumed that both species share the same energy spectrum of the p band and hence $\psi_{\mathbf{K}_{1,2}}$ due to a totally symmetric setting. However, such a degeneracy is lifted when imbalance in the atomic mass or population occurs that $\psi_{\mathbf{K}_{1,2}}$ turn out to be species dependent.
[38] The SU(2) rotations are defined as $\hat{R} = \exp(-i\phi\hat{\boldsymbol{\sigma}} \cdot \mathbf{n}/2)$, with ϕ the rotation angle around $\mathbf{n}$ and $\hat{\boldsymbol{\sigma}}$ the Pauli vector.
[39] E. Altman, W. Hofstetter, E. Demler, and M. D. Lukin, New J. Phys. **5**, 113 (2003).
[40] T. Mishra, R. V. Pai, and B. P. Das, Phys. Rev. A **76**, 013604 (2007).
[41] F. Zhan and I. P. McCulloch, Phys. Rev. A **89**, 057601 (2014).
[42] F. Lingua, M. Guglielmino, V. Penna, and B. C. Sansone, Phys. Rev. A **92**, 053610 (2015).
[43] S. Machluf, Y. Japha, and R. Folman, Nat. Commun. **4**, 2424 (2013).